

Space Weather®

M

RESEARCH ARTICLE

10.1029/2024SW004237

Key Points:

- We develop a real-time regional Total Electron Content (TEC) map service, which achieves the construction of a high-precision, real-time TEC map
- The Recurrent Feature Reasoning (RFR) and Knowledge Consistent Attention module embedded in RFR-TEC enable the reconstruction of TEC maps with refined details, even under high data missing rates
- Experimental results demonstrate that the proposed real-time RFR-TEC improves performance by 47.8% over post-processed and real-time GIMs

Correspondence to:

Q. Kong and B. Chen, kongqinglei@hit.edu.cn; hitchenbo@hit.edu.cn

Citation:

Sun, M., Liu, T., Ding, Z., Liu, J., Huang, Y., Zhang, K., et al. (2025). Real-time Regional Ionosphere modeling with RFR-net over China. *Space Weather*, 23, e2024SW004237. https://doi.org/10.1029/2024SW004237

Received 2 NOV 2024 Accepted 1 AUG 2025

Author Contributions:

Conceptualization: Mengfei Sun, Yanshi Huang, Kun Zhang, Qinglei Kong, Ro Chan

Formal analysis: Mengfei Sun Methodology: Mengfei Sun, Tong Liu, Jian Liu, Yanshi Huang, Kun Zhang, Bo Chen

Software: Mengfei Sun, Kun Zhang Validation: Mengfei Sun Writing – original draft: Mengfei Sun,

Qinglei Kong

Writing – review & editing: Mengfei Sun, Tong Liu, Zonghua Ding, Jian Liu, Shengliang Fang, Shizhong Li, Qinglei Kong, Bo Chen

© 2025. The Author(s).

This is an open access article under the terms of the Creative Commons

Attribution License, which permits use, distribution and reproduction in any medium, provided the original work is properly cited.

Real-Time Regional Ionosphere Modeling With RFR-Net Over China

Mengfei Sun^{1,2}, Tong Liu³, Zonghua Ding⁴, Jian Liu^{1,2}, Yanshi Huang¹, Kun Zhang¹, Shengliang Fang⁵, Shizhong Li⁶, Qinglei Kong^{1,2}, and Bo Chen^{1,2}

¹School of Aerospace, Harbin Institute of Technology Shenzhen, Shenzhen, China, ²Key Laboratory of Aerospace RS Big-Data Intelligent Processing and Application of Guangdong Higher Education Institutes, Harbin Institute of Technology, Shenzhen, China, ³The Hong Kong Polytechnic University, Hong Kong, Hong Kong, ⁴National Key Laboratory of Electromagnetic Environment, Qingdao, China, ⁵College of Aerospace Information, Space Engineering University, Beijing, China, ⁶China Centre for Resources Satellite Data and Application, Beijing, China

Abstract The mid-to-low-latitude ionosphere, influenced by phenomena such as the Equatorial Ionization Anomaly, responds more sensitively to changes in solar activity, which negatively affect the transmission of various electromagnetic signals. Moreover, next-generation technologies, particularly Precise Point Positioning-Real-Time Kinematic (PPP-RTK), require more instant and detailed information on near-earth space environments. However, current ionospheric Total Electron Content (TEC) maps are often post-processed and designed for global applications. Under this challenge, we develop a real-time, high-precision regional ionospheric TEC map service using a deep learning inpainting Recurrent Feature Reasoning (RFR) method. Given the limited ionospheric observation resources, our approach significantly reduces the scale of observational data by utilizing only 2.5% of the total TEC data. This is achieved through the RFR and the Knowledge Consistent Attention (KCA) module embedded in the RFR-TEC model, where the RFR module leverages pixel correlations for robust estimation, and the KCA mechanism enforces patch consistency. Results indicate that the real-time RFR-TEC achieves TEC accuracy comparable to the post-processed CODE-TEC and surpasses the real-time UPC-TEC by 47.8% in long-term validation. Additionally, the RFR-TEC map demonstrates superior stability compared to the real-time UPC-TEC, while its performance varies with the seasons.

Plain Language Summary The mid-to-low-latitude ionosphere's response to solar activity impacts electromagnetic signal transmission. Next-generation technologies particularly PPP-RTK require real-time, detailed near-earth space environment data. We developed a real-time, high-precision regional Total Electron Content (TEC) map service using a deep learning method called RFR-TEC. This approach utilizes only 2.5% of the total TEC data yet achieves superior accuracy compared to existing methods, improving TEC accuracy by up to 47.8% in long-term validation. Furthermore, it demonstrates superior stability compared to the real-time UPC-TEC.

1. Introduction

The mid-to-low-latitude ionosphere is highly sensitive to solar activity, such as storms and flares (Forbes et al., 2000). Variations in the ionosphere can significantly affect the transmission of electromagnetic signals, reducing the accuracy of satellite navigation systems, disrupting high-frequency communications, and degrading radar system performance (Mannucci, Iijima, Lindqwister, et al., 1999). To describes the ionosphere's state, the Total Electron Content (TEC) is a critical parameter, which represents the integration of electron density along the satellite signal path (Banville & Langley, 2013; Vadakke Veettil et al., 2020). Due to its high accuracy, global coverage, and continuous all-weather monitoring capabilities, Global Navigation Satellite System (GNSS) observation data is the most widely used method for obtaining TEC (Chen et al., 2018). The developed ionospheric TEC maps facilitates a plenty of relevant fields, including GNSS positioning, ionospheric delay in remote sensing applications, space weather monitoring, satellite communication and climate change studies (Banville et al., 2014; Jehle et al., 2009; Kong et al., 2023, 2024; Tariq et al., 2019). However, the current TEC maps struggle to meet the demanding requirements of established applications like PPP-RTK (Li et al., 2022; Pan et al., 2022), and they also limit progress in research areas such as the study of potential ionospheric precursors to major geophysical events (Eshkuvatov et al., 2023; Lim & Leong, 2019).

SUN ET AL. 1 of 16

From the perspective of processing timeliness, ionospheric TEC maps can be categorized as either postprocessed or real-time. The post-processed Global Ionospheric Map (GIM) was initially developed by organizations such as the International GNSS Service to enhance GPS positioning accuracy, using grid-based and function-based methods to achieve a global TEC map with a spatial-temporal resolution of 2.5° by 5° per hour (Hernández-Pajares et al., 2011; Roma-Dollase et al., 2018). Later, multiple institutions provide GIM products, including the Center for Orbit Determination in Europe (CODE), Jet Propulsion Laboratory (JPL), and Universitat Politècnica de Catalunya (UPC) (Hernández-Pajares et al., 1999; Mannucci et al., 1998). With the recent booming in generative adversarial networks (GAN), the image completion algorithm is gradually applied to TEC field since the TEC maps can be regarded as 2D images. Chen et al. (2019) first applied deep convolutional GAN (DCGAN) and regularized DCGAN (R-DCGAN) to complete missing VTEC data from the MIT Haystack Madrigal data set, effectively representing ionospheric peak structures under varying conditions. Pan et al. (2020, 2021) improved the DCGAN by combined with poisson blending and spectrally normalized patch, which effectively learning the completion process for IGS-TEC maps. Chen et al. (2021) also proposes a new global and local Gan (GLGAN) method based on DCGAN, which uses two discriminators to improve the quality of the output image and the precision of the network. Most of these GAN-based models are based on the post-processed GIM, but the GIM typically use a 3- or 7-day window to calculate the middle day's products, resulting in an 11-day delay for the final product. The post-processing methods do not satisfy real-time space applications that require the current state of the ionosphere. For instance, real-time precise positioning requires immediate ionospheric TEC delay data to ensure accuracy and stability and the study of potential ionospheric precursors to major geophysical events needs TEC data at least 0-24 hr in advance for effective monitoring (Eshkuvatov et al., 2023; Pan et al., 2022).

The real-time TEC maps are categorized into global and regional maps based on the functioning area. To fulfill the requirements of real-time application needs, institutes such as UPC, the Center National d'Études Spatiales (CNES), and the Chinese Academy of Sciences have developed real-time global coverage GIMs by integrating ionospheric TEC forecasting models with GNSS observation data. The global real-time TEC maps generally describe the average state of the ionosphere at large scales, and it is difficult to reflect the fine ionospheric characteristics of different regions for precise intra-regional applications. Particularly, these TEC maps are usually designed for global research and application, for example, the low-precision GNSS pseudorange singlepoint positioning and global space weather research, which have low spatial-temporal resolution and precision. Real-time regional ionospheric maps can provide greater accuracy and details for the unique ionospheric characteristics of different regions. They concentrate on the land area of middle and low latitudes, which need a lot of observation data to support, and use different methods. For Australian area, Liu, Zhang, et al. (2018) used 30 uniformly distributed GNSS stations with PPP-derived slant ionospheric delays for real-time TEC mapping. Li et al. (2019) developed a regional ionospheric map suitable for real-time positioning using a two-layer spherical harmonic approximation method based on data from 24 stations in Australia. For South America, Mendoza et al. (2019) utilized data from over 200 ground-based stations to establish a Near-Real-Time Ionospheric TEC Monitoring System. Silva et al. (2023) developed an ANN based on a multilayer perceptron approach to map TEC in low-latitude Brazil. For china region, Liu et al. (2011) presented a spherical cap harmonic model for regional TEC mapping using data from approximately 40 stations in China over one year. Song and Shi (2024) used multisource data, including 257 stations, and utilized a particle swarm optimization neural network to reconstruct the ionospheric TEC map over China. To cater to the requirements of high-precision real-time GNSS positioning, high-quality low-latency satellite internet communications, and early warning systems for natural disasters like earthquakes, which are deployed globally, there is an essential need for ionospheric TEC models that are effective across all regions. However, geographic and political constraints in certain areas have led to limited data availability, thus complicating the development of TEC models using traditional methods. Therefore, it is imperative to develop an innovative approach for constructing regional TEC maps under conditions of restricted input data.

Given the above challenges, the goal is to develop a real-time regional ionospheric TEC map service, which is characterized by achieving high-precision presentation with limited data. In particular, the contributions of this article are as follows.

 We develop a real-time regional TEC map service, which achieves the construction of a TEC map with limited observation data. Particularly, the service can generate TEC maps in real-time by combining GPS observation data with the RFR-TEC model.

SUN ET AL. 2 of 16

wiley.com/doi/10.1029/2024SW004237 by HONG KONG POLYTECHNIC UNIVERSITY HU NG HOM, Wiley Online Librar

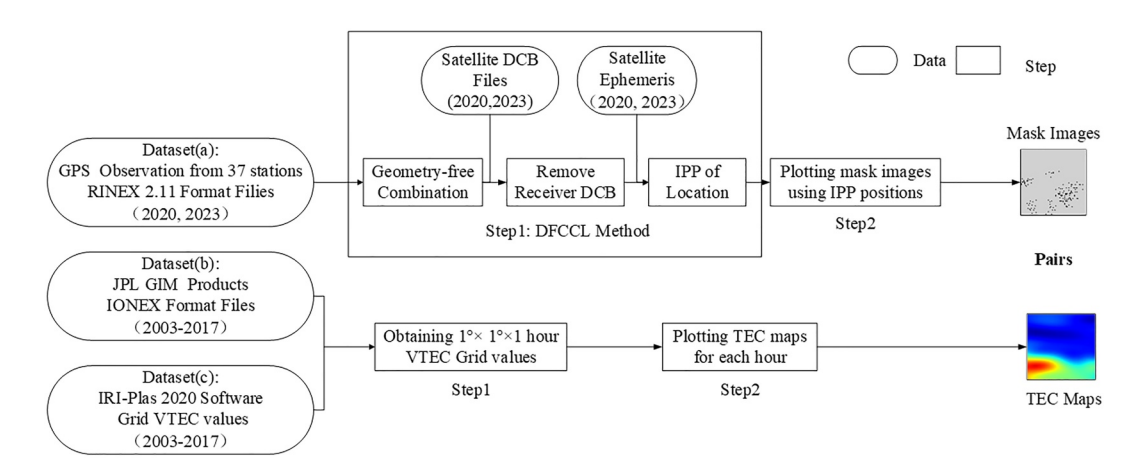


Figure 1. Training data generation process.

- 2. We also construct the RFR-TEC model to convert discrete inputs into regular grid TEC. First, the RFR-TEC model enables the generation of TEC maps with limited and distant data inputs, by exploiting recursive inference and a specialized attention mechanism. Second, to guarantee the accuracy of TEC maps, the RFR-TEC model keeps the origin TEC data input in the result derived.
- 3. To evaluate the performance of the TEC map, we designed two experiments to validate its performance on both daily and long-term scales. The evaluation results show that our real-time RFR-TEC map achieves better TEC accuracy than the post-processed CODE-TEC and real-time UPC-TEC GIMs and demonstrates superior stability.

The remainder of this paper is organized as follows: In Section 2, we describe the development process of the real-time regional TEC map service. In Section 3, we outline the experimental setup and present the results, evaluating the proposed ionospheric map service by comparing its TEC accuracy with CODE-TEC and real-time UPC-TEC GIMs. In Section 4, we conclude with a summary of key findings and propose potential directions for future research.

2. Construction for Real-Time Regional TEC Map Service

In this section, we first show the preparation of training data in Section 2.1, and present the construction of the RFR-TEC network in Section 2.2. In Section 2.3, we describe the real-time regional TEC map service.

2.1. Training Data Preparation

The training data includes three data sets: (a) regional TEC mask data set derived from observation files in RINEX 2.11 format from 37 GPS stations in 2020 and 2023 (Hu et al., 2001; Kouba, 2009), (b) JPL GIM TEC data set extracted from JPL GIM IONEX format files from 2003 to 2017 (Mannucci, Iijima, Sparks, et al., 1999), and (c) IRI-Plas 2020 TEC data set computed using grid VTEC from IRI-Plas 2020 software (Bilitza et al., 2014, 2017, 2022), as shown in Figure 1. To enhance model robustness and generalization, we augment our training data by integrating two complementary sources: the JPL GIM TEC (data set b), which is fitted to observational data, and the IRI-Plas 2020 TEC (data set c), an empirical model. This combined-data approach ensures our model's predictions are consistent with observations while remaining plausible in data-sparse regions, thereby mitigating the risk of overfitting (R. Zhang et al., 2025). In particular, we design the regional mask data set for TEC map completion for data set (a), which utilizes discrete IPPs positions from GPS data to generate mask images. For data sets (b) and (c), we exploit VTEC values at grid points to generate TEC maps. Each TEC map from data sets (b) and (c) is randomly paired with one of the mask images from data set (a) to form an independent training sample for the subsequent training process.

We build Regional TEC Mask Data set from the observations recorded by 37 GPS stations, whose details are described in Table 1 (Hu et al., 2001; Kouba, 2009). The goal we build this data set is to identify regions that require TEC reconstruction, which symbolized as blank areas. The first step exploits the Dual-Frequency Carrier-to-Code Leveling (DFCCL) method, which couple GPS observations with satellite ephemeris and Differential

SUN ET AL. 3 of 16

Table 1

10.1029/2024SW004237

Establishment							
RINEX ID	Latitude [°]	Longtitude [°]	Height [m]	RINEX ID	Latitude [°]	Longtitude [°]	Height [m]
AIRA	31.8240	130.5995	314.64	PIMO	14.6357	121.0777	95.532
HKKS	22.3679	114.3119	44.7180	POL2	42.6798	74.6943	1,714.2
HKKT	22.4449	114.0665	34.5764	PTAG	14.5354	121.0407	86.65
HKLM	22.2189	114.1200	8.5536	PTGG	14.5354	121.0412	130.2
HKLT	22.4181	113.9966	125.9221	SGOC	6.8920	79.87417	-78.5
HKMW	22.2558	114.0031	194.9461	SIN1	1.34298	103.6794	92.54
HKNP	22.2490	113.8938	350.6723	T430	22.4947	114.1382	86.65
НКОН	22.2476	114.2285	166.4011	TASH	41.3280	69.29556	439.7
HKPC	22.2849	114.0378	18.1303	TWTF	24.9536	121.1645	203.122
HKQT	22.2910	114.2132	47.57760	USUD	36.1331	138.3620	1,508.619
HKSC	22.3221	114.1411	20.2386	WUHN	30.5316	114.3572	28.2
HKSL	22.3720	113.9279	95.2972	BADG	51.7697	102.2349	811.4
HKSS	22.4310	114.2692	38.7135	CHNN	26.1686	127.8261	97.1522
HKST	22.3952	114.1842	258.7045	CKSV	22.9988	120.2200	59.6
HKTK	22.5465	114.2232	22.5335	CUSV	13.7359	100.5339	76.06
HKWS	22.4342	114.3353	63.7909	DAEJ	36.3994	127.3744	117.037
IISC	13.0211	77.5703	843.7145	CCJ2	27.0675	142.1950	104.214
KIT3	39.1347	66.8854	622.6	HKCL	22.2958	113.9077	7.7136
KYC1	22.2840	114.0763	116.3830				

Details of the 37 GPS Stations Used for Total Electron Content (TEC) Map Service and Regional TEC Mask Data set

Code Bias (DCB) files to compute the discrete locations of IPPs. The DFCCL is a common approach for determining IPPs and TEC, wherein the ionosphere is assumed to be a single thin shell at an altitude of 450 km (Mendoza et al., 2019; B. Zhang, 2016; Zhou et al., 2022). The DFCCL involves: (a) formation of the geometry-free combination to remove frequency-independent terms, (b) elimination of satellite and receiver DCB, and (c) utilization of the projection function to acquire IPP locations and VTEC values. We estimated the receiver DCB from GPS dual-frequency observations by applying the least squares method with the M_DCB software (Jin et al., 2012; Ma & Maruyama, 2003). The second step uses the computed IPP positions to create a series of $1^{\circ} \times 1^{\circ} \times 1$ hr mask images, where the black squares in the mask images indicate existing VTEC values that do not require computation, and the blank areas signal the grid where VTEC values need to be calculated.

The NASA JPL GIM, provides a high-accuracy native product with a resolution of $1^{\circ} \times 1^{\circ} \times 1$ hr, offering superior spatial and temporal resolution compared to other agency GIM products, which are generated by combining ground-based GNSS TEC measurements with a climatological model (Mannucci, Iijima, Sparks, et al., 1999). To derive TEC maps, we first obtaining $1^{\circ} \times 1^{\circ} \times 1$ hr VTEC grid values extracted from JPL GIM IONEX files spanning 2003 to 2017, each encapsulating a day's worth of VTEC data. Second, we plot TEC maps for each hour utilizing the acquired VTEC grid values, resulting in approximately 130,000 maps, each depicting the hourly distribution of VTEC.

The IRI-Plas 2020 Model, is the most widely used empirical model that is verified to reflect a better TEC distribution, which is an extension of the International Reference Ionosphere model, incorporates a plasmasphere component that calculates electron density up to the medium earth orbit of GPS satellites, reaching an altitude of 20,000 km (Bilitza et al., 2014, 2017, 2022; Gulyaeva & Bilitza, 2012). In addition to the JPL GIM, TEC maps are also generated using the IRI-Plas 2020 Model. First, we calculated the VTEC at each grid point using the IRI-Plas 2020 software, which offers a spatiotemporal resolution of $1^{\circ} \times 1^{\circ} \times 1$ hr. Second, we produce a data set of IRI-Plas 2020 TEC maps, encompassing approximately 130,000 hourly maps.

SUN ET AL. 4 of 16

wiley.com/doi/10.1029/2024SW004237 by HONG KONG POLYTECHNIC UNIVERSITY HU NG HOM, Wiley Online Library on [06/11/2025]

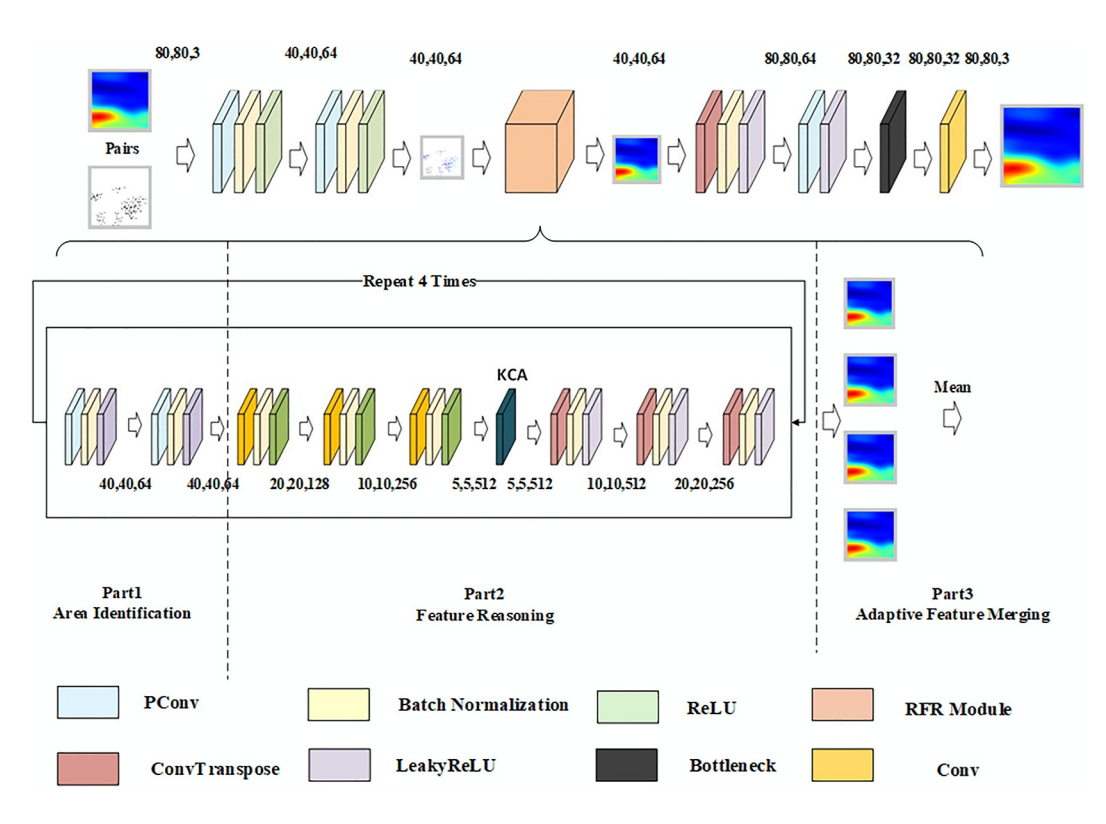


Figure 2. The architecture of the RFR-TEC model.

2.2. Construction of RFR-TEC Network

In this subsection, we exploit Recurrent Feature Reasoning (RFR) network to build RFR-TEC model, which primarily comprises an RFR module and a Knowledge Consistent Attention (KCA) module (J. Li, Wang, Zhang, et al., 2020). The implementation is carried out using PyTorch (Paszke et al., 2019). The RFR module recurrently infers the boundaries of missing areas in convolutional feature maps and uses this information to facilitate superior restoration of more distant regions within incomplete images. This process is similar to the spatial characteristics of TEC, where the accuracy of estimations decreases with increasing spatial distance from the input TEC data. By using the RFR module, we initially calculate grid values near known TEC data and utilize these results as supplementary information to address more remote areas. The KCA module adaptively integrates recurrence scores and ensures consistency in the patch-swapping process, which is particularly effective for images requiring substantial completion. This parallels the iterative nature required in modeling with limited TEC data, ensuring consistency in TEC map computations through multiple cycles to generate a comprehensive model. Moreover, RFR-TEC model preserves the original input values, that is the VTEC, thereby enhancing the accuracy of TEC estimations.

The structure of the RFR-TEC model is depicted in Figure 2. The model takes two images as input: a TEC map and a mask. First, the images pass through two partial convolution layers, a specialized technique designed to handle two images with mask effectively (G. Liu, Reda, et al., 2018). Second, the images are fed into the RFR module, whose details will be shown in the following paragraph. Third, the images sequentially pass through a transposed convolution layer, implemented in PyTorch using the torch.nn.ConvTranspose2d function, followed by another type of partial convolution layer. Fourth, the images flow through a bottleneck layer and a convolution layer to produce the output. Every layer within the network encompasses a combination of convolution operations, batch normalization, and an activation function. The network architecture is designed to reduce and then restore the image size, ensuring that the final output retains the same dimensions as the initial input.

As illustrated in the lower half of Figure 2, the RFR Module primarily composes of three parts. First, the Part 1 (area identification part) is utilized to detect the regions in the TEC map that require inference in each cycle, which consists of the first two partial convolution layers. Second, the Part 2 (feature reasoning part) infers the

SUN ET AL. 5 of 16

content of the identified areas, which includes three subsequent convolution layers, a KCA module, and three transposed convolution layers. The algorithm used in the KCA layer will be described in the following paragraph. The first two parts are executed multiple times in a cycle, and their outputs serve as inputs for the Part 3 (feature merging), whose role is to integrate the intermediate feature maps and ultimately produce the final feature maps.

The KCA is an attention module designed to enhance feature quality in image inpainting. Building on the foundation laid by Yu et al. (2018), KCA addresses the limitations of traditional attention mechanisms, where scores are calculated independently. Instead, it accumulates scores proportionally from previous recurrences, resolving discrepancies when synthesized feature maps are merged. This effectively manages inconsistencies within attention feature maps and offers a more coherent integration of texture features from the background to fill in missing areas, leading to improved image inpainting results. In this context, attention scores represent the focus on different regions or features within the TEC images, guiding the model to concentrate on crucial areas when computing unknown grid points, thereby enhancing accuracy and performance. The detailed computational process is as follows (Yu et al., 2018).

KCA calculates the similarity between each position and every other position in the feature map using convolution operations, thereby generating attention scores. The similarity is computed by:

$$Si_{x,y,x,y'} = \left\langle \frac{f_{x,y}}{\|f_{x,y}\|}, \frac{d_{x,y'}}{\|d_{x,y'}\|} \right\rangle$$
 (1)

where $Si_{x,y,x,y'}$ represents the similarity between the feature vectors located at missing pixels (foreground) (x,y) and surroundings (background) (x,y') in TEC map, $f_{x,y}$ denotes the feature vector at location (x,y) in the feature map, $\|\cdot\|$ indicates the L2 norm, $\langle\cdot,\cdot\rangle$ represents the inner product operation, used to compute the similarity between two normalized feature vectors.

This convolution operation is implemented in code using torch.nn.functional.conv2d() from PyTorch, resulting in:

$$conv_{result} = Si_{r,v,r'v'} \tag{2}$$

The Softmax operation is applied to the convolution result conv_{result} using torch.nn.functional. softmax to generate attention scores att_{scores}. The Softmax operation converts the similarities into a probability distribution, reflecting the degree of attention each position pays to others.

$$att_{scores} = F.softmax(conv_{result}, dim = 1)$$
(3)

where att_{scores} represents the attention score matrix, F.softmax denotes the Softmax operation, and dim specifies the channel dimension. If previous attention scores att_{scores-prev} and masks masks_{prev} are available, the adjustment is made using the equation:

$$\mathsf{att}_{\mathsf{scores}} = \frac{\mathsf{att}_{\mathsf{scores-prev}}(i:i+1) \times \mathsf{masks}_{\mathsf{prev}}(i:i+1) + \mathsf{att}_{\mathsf{scores}} \times \mathsf{ratio}}{\mathsf{masks}_{\mathsf{prev}}(i:i+1) + \mathsf{ratio}} \tag{4}$$

Loss Analysis. The loss function of RFR-TEC model consists of perceptual loss and style loss, comparing the difference between the deep feature map of the generated TEC map and the input TEC map. The perceptual loss $L_{perceptual}$ is represented as follows:

$$\mathsf{L}_{\mathsf{perceptual}} = \sum_{i=1}^{N} \frac{1}{H_i W_i C_i} \left| \phi_{\mathsf{pool}_i}^{\mathsf{input}} - \phi_{\mathsf{pool}_i}^{\mathsf{out}} \right|_1 \tag{5}$$

where H_i , W_i , C_i represent the height, weight and channel size of the *i*th feature map, respectively. ϕ_{pool_i} denotes the feature maps from the *i*th pooling layer. The subscripts input and out denote the complete TEC map input and the TEC map output by the model, respectively. Similarly, the style loss is expressed as:

SUN ET AL. 6 of 16



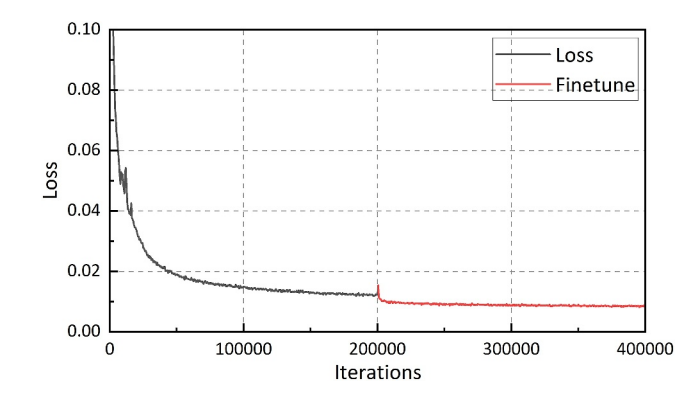


Figure 3. The variation of loss during the training process.

$$\mathsf{L}_{\mathsf{style}} = \sum_{i=1}^{N} \frac{1}{C_i \times C_i} \left| \frac{1}{H_i W_i C_i} (\phi_{\mathsf{pool}_i}^{\mathsf{style}_{input}} - \phi_{\mathsf{pool}_i}^{\mathsf{style}_{out}}) \right|_1 \tag{6}$$

The total loss is expressed as:

$$L_{total} = \lambda_{hole} L_{hole} + \lambda_{valid} L_{valid} + \lambda_{style} L_{style} + \lambda_{perceptual} L_{perceptual}$$
 (7)

where L_{hole} and L_{valid} represent L1 differences in the unmasked area and masked area, respectively. The symbol λ represents a constant coefficient.

In the RFR-TEC model, a dedicated validation set was not delineated. In fact, it is common practice in image inpainting algorithms to forgo separating a validation set (Yu et al., 2018; J. Li, Wang, Zhang, et al., 2020). The training and optimization process can be succinctly described as follows: (a) The

RFR-TEC model acquires real TEC maps along with masks as inputs through a data loader (as illustrated in Figure 2), (b) During the forward pass, the model generates inpainted images. The aggregate loss is computed by applying various loss functions (e.g., style loss, perceptual loss) on these generated images in conjunction with the authentic TEC maps and (c) Generator parameters are updated via backpropagation to optimize the model performance. Figure 3 illustrates the fluctuation of loss throughout the training phase. Initially, the model underwent training for 200,000 iterations, followed by 200,000 fine-tuning iterations, which were pivotal for optimization and adaptation, thereby enhancing the model's performance on specific tasks and data sets.

2.3. Real-Time Regional TEC Map Service

With the RFR-TEC model derived from Section 2.2, the method can be used to build high-precision real-time regional TEC model. As depicted in Figure 4, the real-time GPS observation data and products are processed through the DFCCL algorithm to extract discrete IPP locations and VTEC values, which are then plotted on an incomplete TEC Map. The real-time data and products used for real-time TEC modeling includes GPS observations from 37 stations as described in Table 1, satellite broadcast ephemeris files corresponding to the observation times, and Satellite DCB files, whose detailed description is provided in Table 2. Furthermore, the incomplete TEC map is processed through the trained RFR-TEC Model to generate complete TEC maps.

3. Experiments and Results

In this section, we initially describe the experimental setup in Section 3.1, including details on the experiment time, the experiment region, the reference truth TEC used for comparison, and the evaluation metrics. Since ionospheric variations are spatially and temporally correlated, we evaluate the diurnal variations of the TEC map using the spatially extensive MIT Madrigal database in Section 3.2. In Section 3.3, we conduct year-long experiments using seven reference GPS stations to validate the long-term performance and seasonal variations of TEC maps.

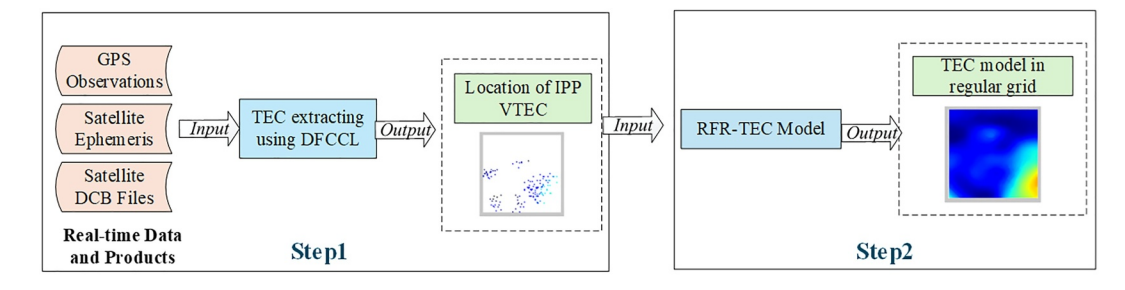


Figure 4. Real-time regional Total Electron Content model service process.

SUN ET AL. 7 of 16

	The Data and Products Usea in Real-1	Data and Products Osea in Real-Time Total Electron Content Modeling			
Items		Strategies			
	Observations	GPS L1/L2 raw observations			
		GPS P1/P2 raw observations			
	Sampling rate	30 s			
	Elevation cutoff	15°			
	Orbits and Clocks	Broadcast ephemeris			
	Satellite DCB	CAS 1-day predicted DCBs			

3.1. Experiment Description

Experimental setup. The experimental period includes DOY 047, 2020, and DOY 005, 2023, for the diurnal variation evaluation in Section 3.2, and the entire year of 2020 for the long-term quantitative evaluation in Section 3.3. Figure 5 shows $Kp \times 10$ (level of geomagnetic activity) and F10.7 (level of solar activity), while Figure 6 displays the Dst indices (indicating geomagnetic storm intensity) for the 2-day experimental periods and the entire year of 2020.

The experiment region covers China and the surroundings, spanning longitudes from 65 to 145° E and latitudes from 0 to 80° N. Each TEC map is structured into an 80×80 grid, comprising a total of 6,400 grid points. As

illustrated in Figure 7a, the known limited TEC data computed from 37 GPS ground stations (red dots) cover approximately 100 grid points (blue dots) (Hu et al., 2001; Kouba, 2009), whereas 97.5%–98.5% of the points required computational inference. Additionally, the green triangles in the figure represent the seven stations used as reference stations for the quantitative evaluation of the TEC maps. Table 3 provides detailed information about these reference stations.

Evaluation Metrics for TEC Map. We evaluate the TEC map using two approaches: (a) Diurnal evaluation based on the MIT Madrigal database for Section 3.2. The MIT-TEC data, primarily derived from automated processing of data collected by approximately 5,000 ground-based GPS stations worldwide and provided with a spatial and temporal resolution of $1^{\circ} \times 1^{\circ} \times 15$ min, is obtained from the MIT Madrigal database and has been utilized as a reference in several studies (Aa et al., 2015; Mendoza et al., 2019; Rideout & Coster, 2006). In this study, we use a resolution of $1^{\circ} \times 1^{\circ} \times 1$ hr. A sample MIT-TEC map for the study region at a single time point is shown in Figure 7b, with approximately 1,000 data points. (b) Quantitative long-term evaluation using the reference stations for Section 3.3. To quantitatively assess the accuracy of the TEC map, we selected seven stations that did not participate in the TEC map construction and calculated VTEC values for elevation angles greater than 60° using the DFCCL method mentioned in Section 2.1 as reference TEC. The specific locations and information of the seven reference stations are described in Figure 7a and Table 3.

Equations 8 and 9 describes the calculation method for the "diff" values of TEC difference maps shown on the right side of Figures 8 and 9 for evaluation method (a), where VTEC_{diff} represents the absolute difference between the MIT VTEC and the model TEC at the corresponding grid points:

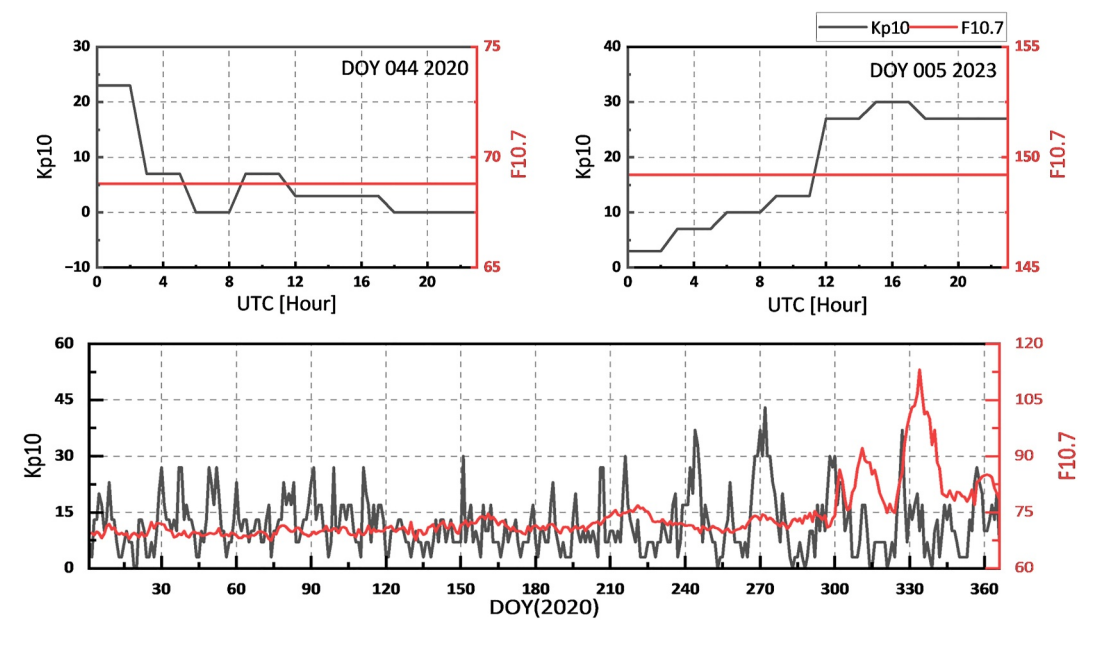


Figure 5. The variations in $Kp \times 10$ and F10.7 indices during the experimental period.

SUN ET AL. 8 of 16

15427390, 2025, 8, Downloaded from https://agupubs.onlinelibrary.wiley.com/doi/10.1029/2024SW004237 by HONG KONG POLYTECHNIC UNIVERSITY HU NG HOM, Wiley Online Library on [06/11/2025].

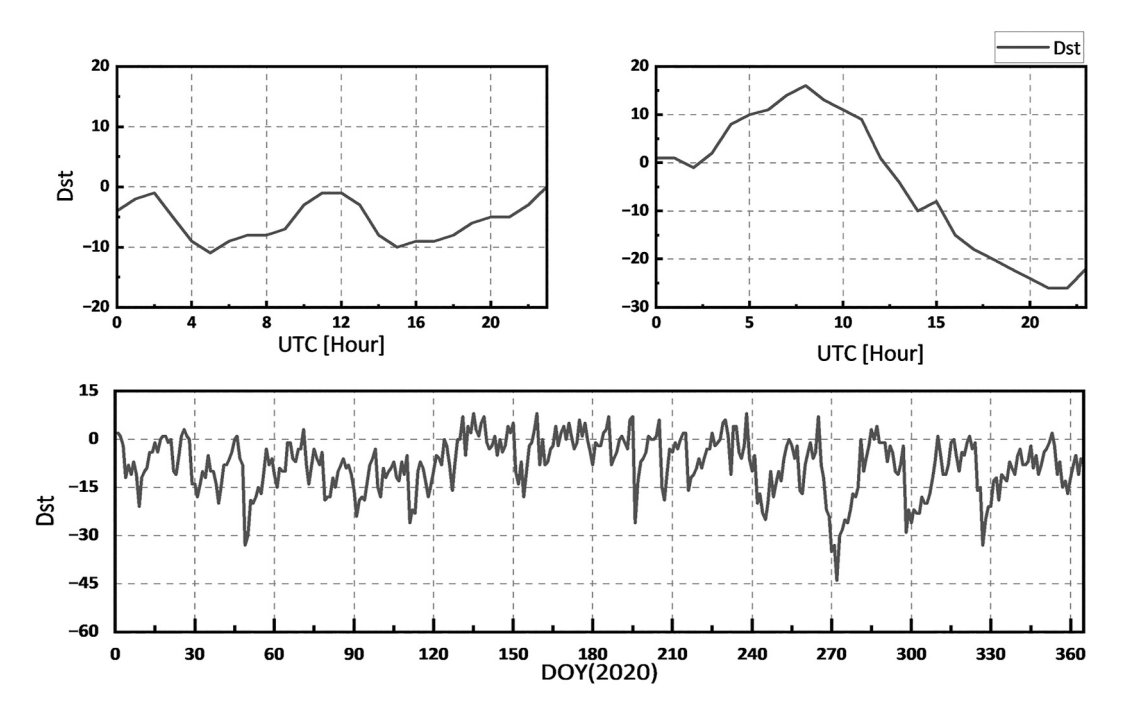


Figure 6. The variations in Dst indices during the experimental period.

$$VTEC_{diff} = |VTEC_{MIT} - VTEC_{Map}|$$
 (8)

$$\mathsf{Map} \in \{\mathsf{RFR} - \mathsf{TEC}, \mathsf{CODE} - \mathsf{TEC}, \mathsf{UPC} - \mathsf{TEC}\} \tag{9}$$

where $VTEC_{MIT}$ represents the values at the grid points of the reference TEC model, while $VTEC_{Map}$ represents the values at the grid points of the model TEC, which includes the RFR-TEC, CODE-TEC, and UPC-TEC models in this study. The symbol $|\cdot|$ denotes the absolute value operation.

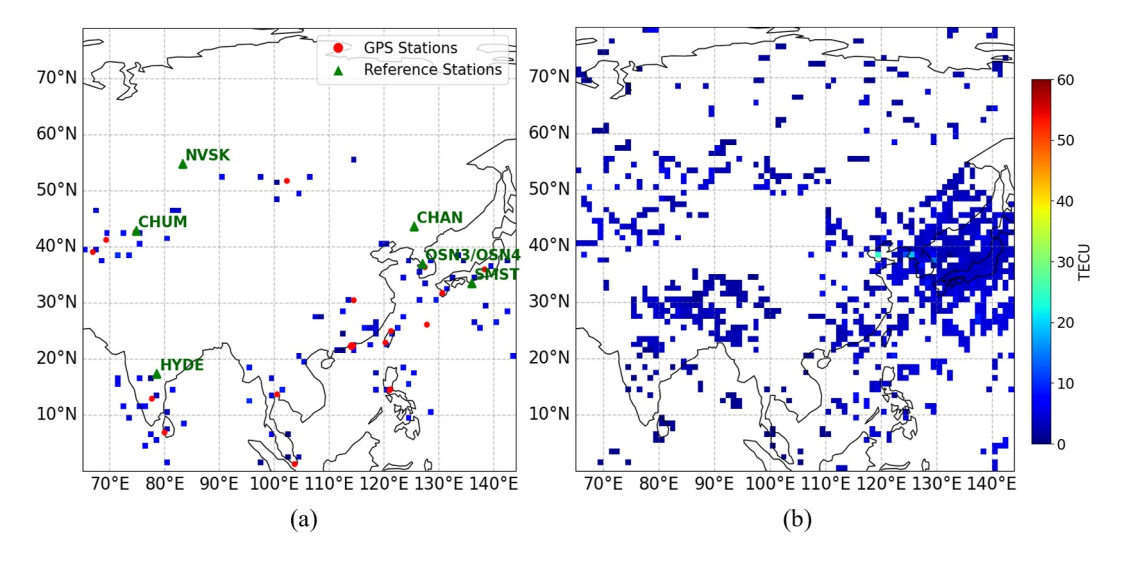


Figure 7. Map of the study area at 23:00 UTC on DOY 2020047: (a) Illustration of an Incomplete Total Electron Content (TEC) Map. (b) Diagram of Reference TEC (MIT-TEC).

SUN ET AL. 9 of 16

Table 3Detailed Description of the Seven GPS Stations Used for Validation

RINEX ID	Latitude [°]	Longtitude [°]	Height [m]
CHAN	43.7905	125.4433	268.3
CHUM	42.9985	74.7551	716.3
HYDE	17.4172	78.5508	441.6
NVSK	54.8406	83.2355	123.6
OSN3	37.0826	127.0336	64.4
OSN4	37.0826	127.0336	64.4
SMST	33.5778	135.9369	97.5

The average model accuracy for a given day, VTEC_{mean}, is calculated using the following equation for evaluation method (b). VTEC_{mean} represents the model accuracy over 24 hr for that specific day, and is used in the construction of Figures 10 and 11 (Z. Liu & Gao, 2004; Z. Chen et al., 2022):

$$VTEC_{mean} = \frac{1}{24} \sum_{h=0}^{23} \left(\frac{\sum_{n=0}^{IPPs} VTEC_{stadiff_n}}{IPPs} \right)_h$$
 (10)

$$VTEC_{stadiff} = |VTEC_{STA} - VTEC_{StaMap}|$$
 (11)

where IPPs refers to the number of ionospheric pierce points calculated from the seven reference stations, and h represents the hours. VTEC_{STA} represents the VTEC values calculated from observations at reference stations with

elevation angles greater than 60° . VTEC_{StaMap} denotes the VTEC values obtained by bilinear interpolation from the three TEC maps based on the locations of the IPPs.

3.2. Diurnal Evaluation of RFR-TEC Map Accuracy

The MIT-TEC has a broad spatial distribution, making it suitable for evaluating diurnal TEC variations using method (a). Figure 8 displays TEC and TEC difference maps derived from Equation 8 for DOY 047, 2020 at four specific UTC times: 0:00, 6:00, 12:00, and 18:00. Figure 8a illustrates the TEC maps from RFR-TEC, CODE-TEC, and UPC-TEC alongside MIT-TEC for comparison. Figure 8b delineates the TEC difference maps between the three maps and MIT-TEC. For Figure 8a, it can be observed that the RFR-TEC model exhibits higher TECU than the other two maps, presenting a distinct layered structure that reveals more detail of the ionosphere at 6:00 and 12:00 UTC (which correspond to local times of 14:00 and 20:00, respectively) within low-latitude areas

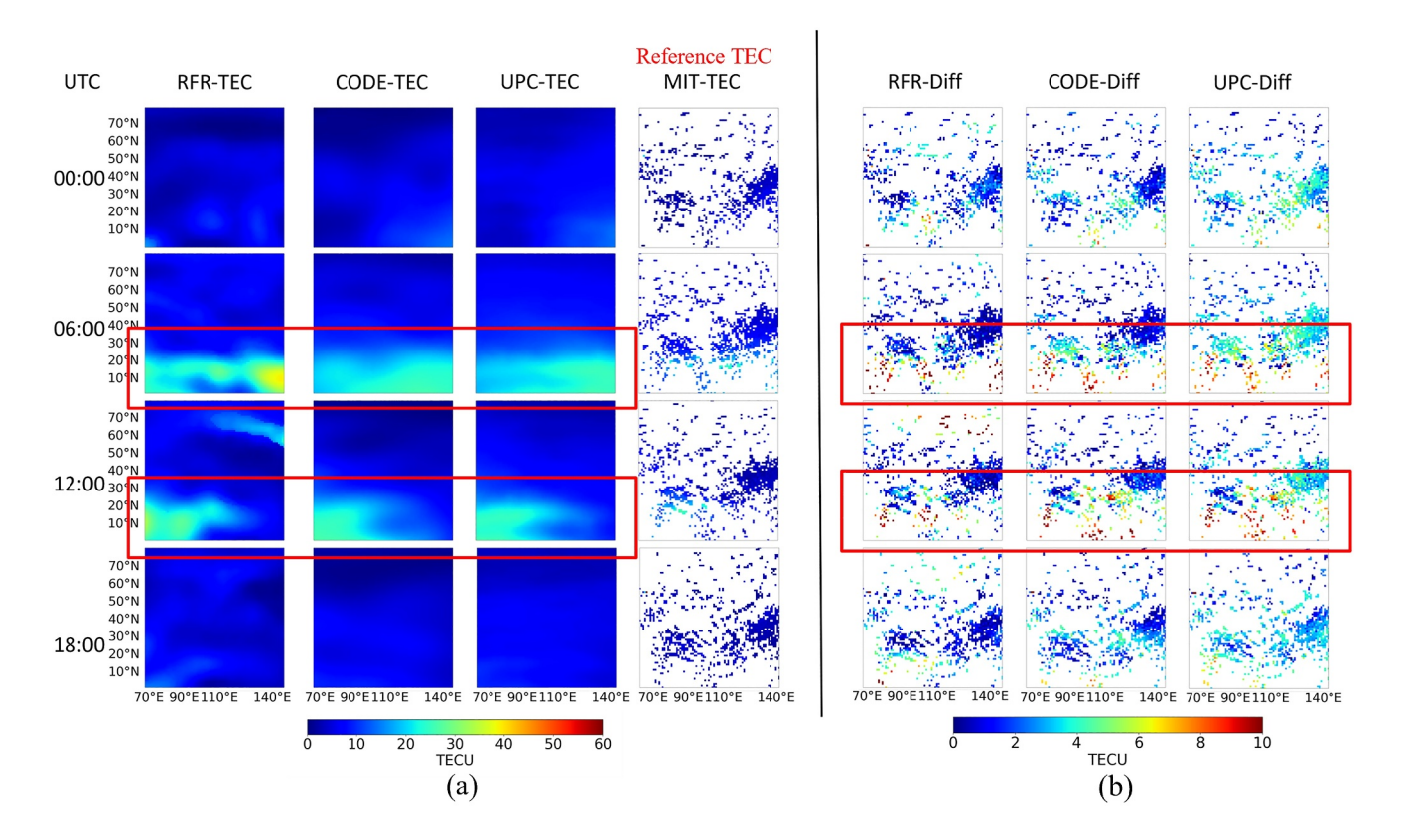


Figure 8. The ionospheric Total Electron Content (TEC) and TEC difference maps for 2020 DOY 047 at UTC 0, 6, 12, and 18 hr. (a) TEC maps of RFR-TEC, CODE TEC, and UPC-TEC, as well as MIT-TEC used as a reference for comparison; (b) TEC difference maps, representing the differences between RFR-TEC, CODE TEC, and UPC-TEC and the reference TEC (MIT-TEC), denoted as RFR-Diff, CODE-Diff, and UPC-Diff, respectively.

SUN ET AL. 10 of 16

15427390, 2025, 8, Downloaded from https://agupubs.online.library.wiley.com/doi/10.1029/2024SW004237 by HONG KONG POLYTECHNIC UNIVERSITY HU NG HOM, Wiley Online Library on [06/11/2025]. See the Terr

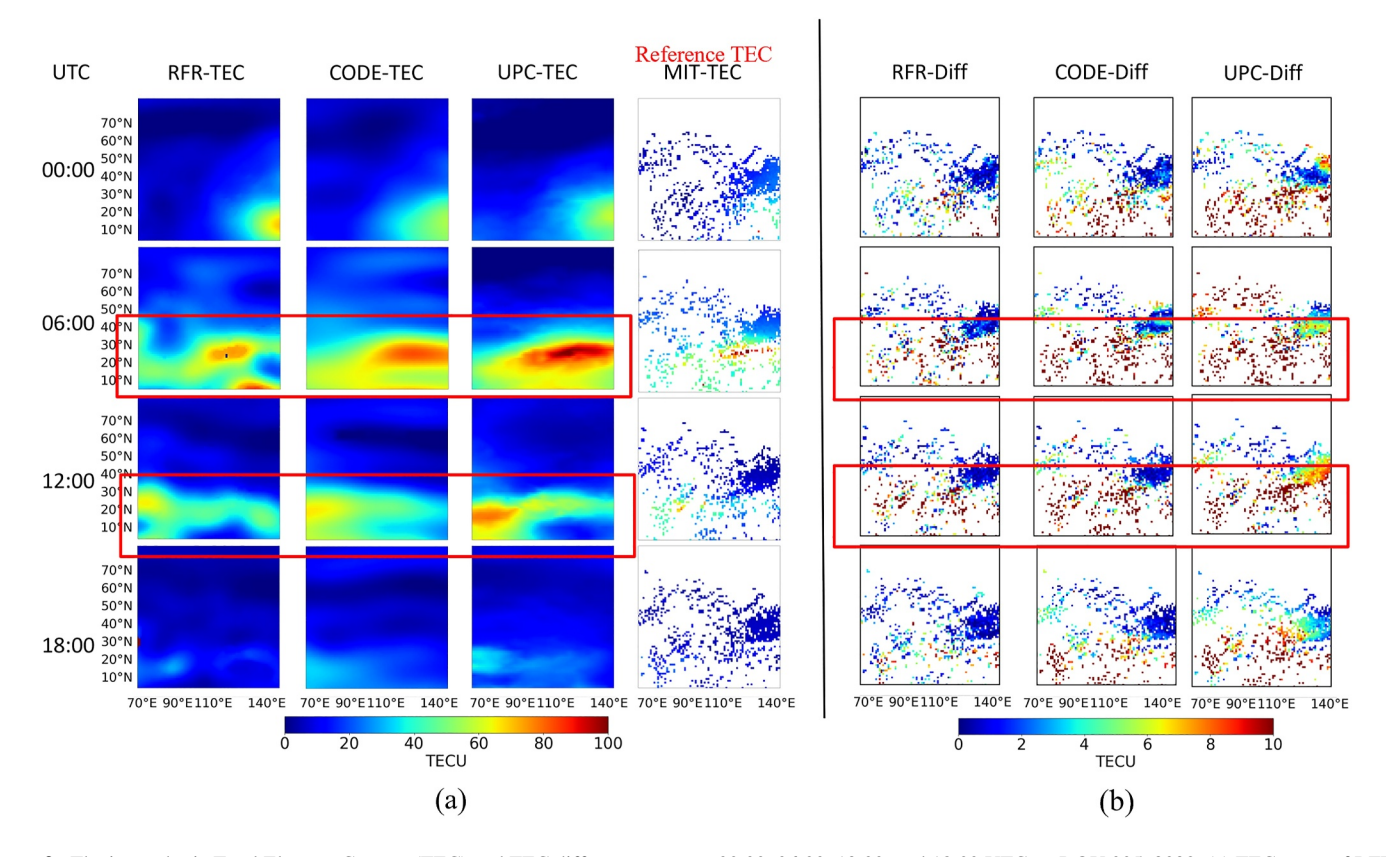


Figure 9. The ionospheric Total Electron Content (TEC) and TEC difference maps at 00:00, 06:00, 12:00, and 18:00 UTC on DOY 005, 2023. (a) TEC maps of RFR-TEC, CODE TEC, and UPC-TEC, as well as MIT-TEC used as a reference for comparison; (b) TEC difference maps, representing the differences between RFR-TEC, CODE TEC, and UPC-TEC and the reference TEC (MIT-TEC), denoted as RFR-Diff, CODE-Diff, and UPC-Diff, respectively.

(highlighted by the red boxes), which indicates that the RFR-TEC model can describe a more detailed state of ionospheric activity. For Figure 8b, colors closer to red indicate a larger discrepancy from the reference TEC, implying lower TEC accuracy, whereas colors closer to blue indicate higher TEC accuracy. Particularly in the regions highlighted by the red boxes, it can be seen that despite having a similar number of red grid points, the RFR-TEC model demonstrates higher accuracy in its other grid points. Overall, the TEC difference maps indicate that RFR-TEC consistently showcases the highest precision. CODE-TEC follows with the second-best level of accuracy, while UPC-TEC exhibits the lowest accuracy among the assessed models. Notably, the gap in accuracy among the maps becomes more pronounced during periods and regions of high ionospheric activity, during which the RFR-TEC map demonstrates superior performance.

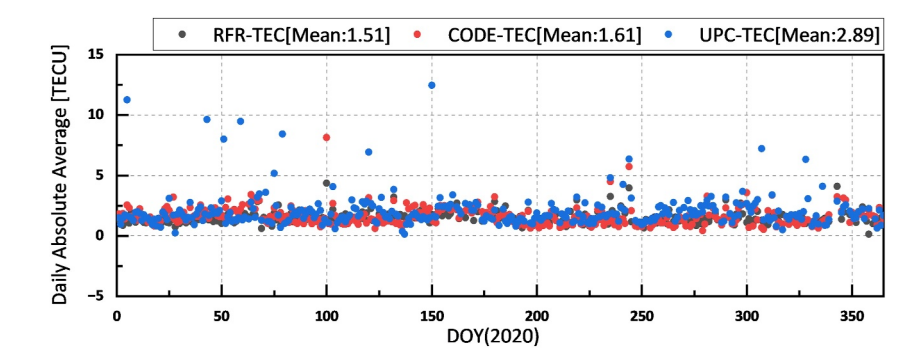


Figure 10. The daily mean differences between the three maps and the reference stations during 2020. For clarity, values exceeding 15 TECU have been excluded from the plot.

SUN ET AL. 11 of 16

15427390, 2025, 8, Downloaded from https://agupubs.onlinelibrary.wiley.com/doi/10.1029/024\$W004237 by HONG KONG POLYTECHNIC UNIVERSITY HU NG HOM, Wiley Online Library on [06/11/2025]. See the Terms and Conditions

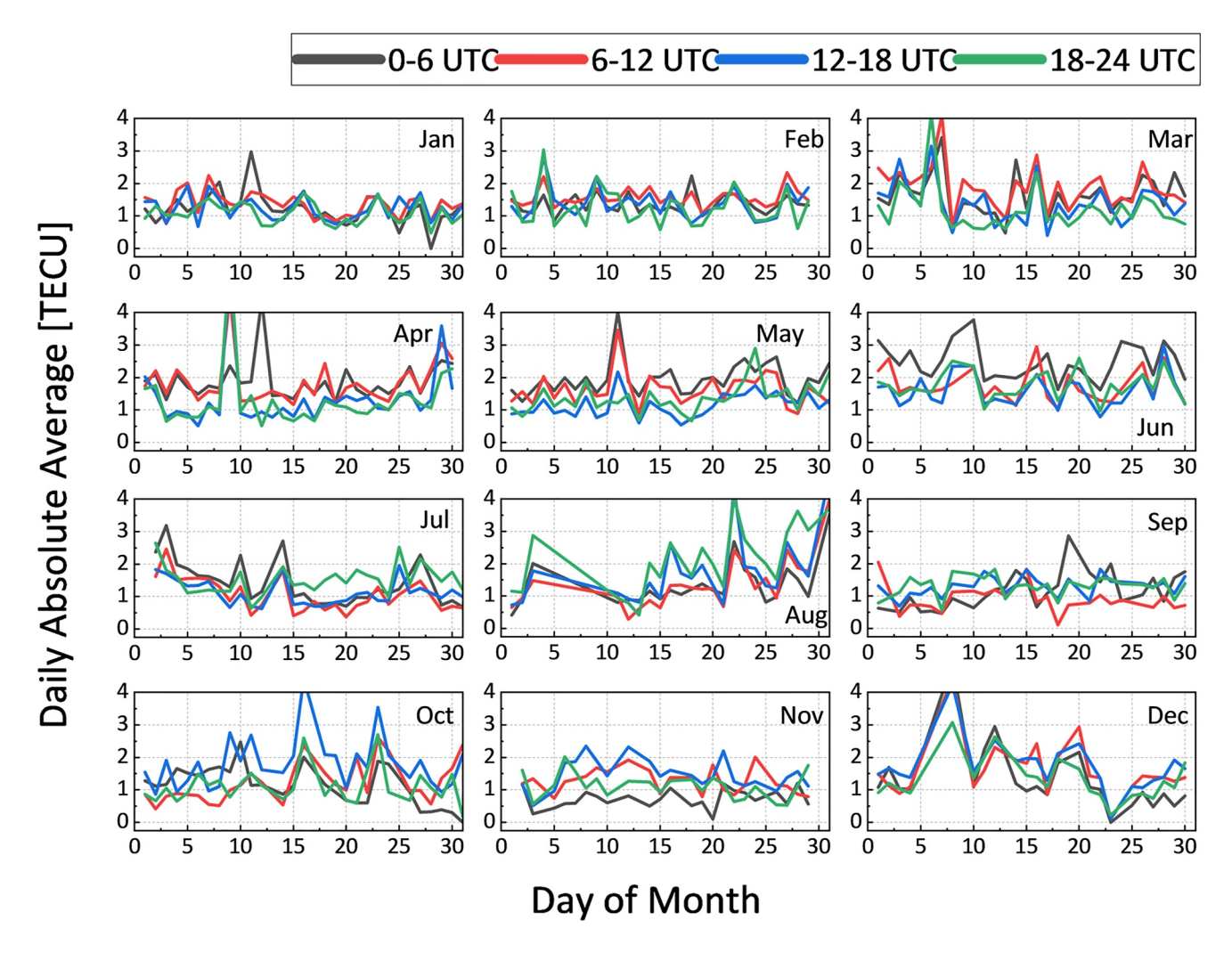


Figure 11. The daily average differences between the RFR-TEC map and reference stations during the year 2020.

Figure 9 presents TEC and TEC difference maps at four distinct UTC instances: 00:00, 06:00, 12:00, and 18:00, on DOY 005 in the year 2023, which convey insights analogous to those presented in Figure 8, focusing on the comparative visualization of ionospheric structures as depicted by different TEC maps. For Figure 9a, it can be observed that the VTEC value for the RFR-TEC map is less uniform, with disparities among the grid points appearing irregularly, which is particularly evident at UTC 06:00 (local time 14:00), one of the day's most active periods for the ionosphere, indicating that the RFR-TEC map can effectively capture fine-scale features and details comparable to real measurement data. For Figure 9b, the RFR-TEC map exhibits fewer grid points with low TEC accuracy (those closer to red) compared to the other two maps, indicating its superior TEC accuracy. This experiment clearly delineates the specific strengths of the RFR-TEC map in representing ionospheric TEC with greater detail and accuracy.

3.3. Long-Term Evaluation of RFR-TEC Map Accuracy

To validate the long-term performance and seasonal variations of RFR-TEC maps, we conducted an evaluation using measured VTEC values from the entire year of 2020. The performance of the proposed TEC map was assessed based on different days of the year, different months, and different times of the day. Figure 10 illustrates the daily average differences between the three maps during the year 2020. The outliers evident in the figure are not artifacts of our validation method but are inherent features of the original data products. For the two real-time TEC maps, the proposed RFR-TEC demonstrates superior stability. While UPC-TEC achieves good accuracy on some days, it exhibits sudden degradation on others, making it difficult to maintain long-term stability. The

SUN ET AL. 12 of 16

respective TEC accuracies are 1.51 TECU and 2.89 TECU, with RFR-TEC achieving an improvement of approximately 47.8% compared to UPC-TEC. In terms of TEC accuracy, the real-time RFR-TEC map performs comparably to the post-processed CODE-TEC map, surpassing it by approximately 6%.

For the long-term evaluation across different months and different times of the day, Figure 11 depicts the absolute mean values of the RFR-TEC map compared to the reference station TEC for different time periods throughout the 12 months of 2020: 18:00–24:00 UTC, 00:00–06:00 UTC, 06:00–12:00 UTC, and 12:00–18:00 UTC. The study area is located in the Northern Hemisphere, with seasons defined as follows: spring (March–May), summer (June–August), autumn (September–November), and winter (December–February). It can be observed that the ionospheric TEC errors are higher in spring and autumn than in summer and winter, with spring errors being greater than those in autumn, consistent with global seasonal variations of the ionosphere (Tulasi Ram et al., 2009). Additionally, the maximum TEC errors in spring occur during the 06:00–12:00 UTC period (14:00–20:00 LT), likely due to variations in solar radiation intensity. In autumn, the errors peak during the 12:00–18:00 UTC period (20:00–04:00 LT), possibly related to the PRereversal Enhancement phenomenon.

4. Discussion

The ionosphere plays a vital role in space weather monitoring and research by influencing communication, navigation, and satellite operations. The primary objective of this study is to develop a high-precision, real-time ionospheric TEC model using limited observational data, thereby addressing a critical gap in real-time ionospheric monitoring and GNSS positioning. Developing a high-precision real-time TEC model with limited data can not only reduce operational costs and improve computational efficiency and responsiveness but also enable timely responses to space weather variations. Furthermore, the model can enhance the accuracy and reliability of communication and navigation systems. We will discuss the RFR-TEC model with other ionospheric modeling techniques from three perspectives: data integration, modeling strategy, and application scenarios.

First, in terms of data integration, the RFR-TEC model stands out due to its ability to function effectively under conditions of extreme data sparsity—a major limitation for many existing methods. Typically, regional ionospheric models require data from approximately 100–200 stations, and previous deep learning-based TEC completion methods have needed at least 30% data availability to perform effectively (Aa et al., 2015; Mendoza et al., 2019; Yang et al., 2022). Most current TEC completion methods, based on GANs and encoder-decoder architectures, are not specifically designed for large-scale data loss scenarios (Chen et al., 2021; Ji et al., 2020; Pan et al., 2020). In contrast, RFR-TEC is specifically designed to operate under extreme data sparsity, demonstrating exceptional tolerance to high data missing rates (e.g., 97.5%–98.5% in this study). This is because the RFR module exploits pixel correlations to enhance deep pixel estimation, thereby improving network performance. Meanwhile, the KCA mechanism ensures patch-swapping consistency, leading to more refined and detailed inpainting results. Consequently, the model is inherently suitable for regions with limited observational coverage.

Second, regarding modeling strategy, the RFR-TEC model employs a data-driven and non-fitting approach. As a data-driven deep learning image completion method, its accuracy relies on the precision of the input TEC data rather than on geographical location. This inherent characteristic, supported by its demonstrated capability to capture ionospheric variations in China's mid-to low-latitude regions—known for significant ionospheric variability—suggests that the model may possess theoretical applicability and generalization potential for regions such as South America, Africa, and other global areas (Development of a Regional GPS-based Ionospheric TEC Model for South Africa, 2007; Takahashi et al., 2016). Moreover, unlike fitting-based models such as most GIM models using Spherical Harmonics, tomography with Kriging, or Generalized Trigonometric Series methods, which modify original TEC values during interpolation, RFR-TEC preserves the integrity of raw measurements throughout the reconstruction process (Hernández-Pajares et al., 2017; Schaer, 1999). This intrinsic design principle is the key factor contributing to the model's robustness and accuracy.

Finally, in terms of application scenarios, RFR-TEC demonstrates broader potential applicability. Many current ionospheric models, such as IRI-2016, NeQuick2, and real-time IGS-GIM, perform poorly in regions with sparse GNSS station coverage—such as oceans, deserts, and polar areas—where data scarcity limits their effectiveness (J. Chen et al., 2020; Durazo et al., 2021; Z. Li, Wang, Hernández-Pajares, et al., 2020). In contrast, RFR-TEC's robustness to missing data makes it particularly suitable for these challenging environments, achieving a 47.8% improvement over the China region. Moreover, RFR-TEC's regional generalization capability supports its global adaptability, rendering it highly valuable for satellite communications, space weather monitoring, and real-time

SUN ET AL. 13 of 16

precise GNSS positioning, where consistent and accurate TEC maps are required across varying spatial and temporal scales.

5. Conclusions

In this study, we successfully developed and validated a real-time regional TEC map service that leverages limited observational data to produce high-precision TEC maps. Central to our approach is the integration of GPS observation data with an innovative Recursive Feature Refinement (RFR)-TEC model designed to optimize the conversion of discrete TEC measurements into uniform grid maps. Key findings include.

- 1. A novel real-time regional TEC mapping service was established, capable of constructing accurate TEC maps even when constrained by limited observational data. This capability is achieved through the synergistic use of GPS observations and the RFR-TEC model, enabling immediate TEC map generation.
- 2. The RFR-TEC model was meticulously crafted to transform sparse and irregularly distributed TEC data points into structured grid maps. This model employs recursive inference techniques alongside a tailored attention mechanism to ensure the precise interpolation of TEC values across the region of interest. Importantly, the original TEC data inputs are preserved in the final output maps, thus maintaining the fidelity of the initial measurements.
- 3. Performance evaluations of diurnal and long-term variations demonstrated significant improvements in TEC map accuracy. Specifically, the RFR-TEC maps achieved an accuracy of approximately 1.51 TECU in long-term validation, representing a 6% improvement over CODE-TEC (1.61 TECU) and a 47.8% enhancement over UPC-TEC (2.89 TECU). Importantly, across all experiments, the RFR-TEC map exhibited superior stability compared to the real-time UPC-TEC, which undoubtedly has positive implications for the application of ionospheric TEC maps. Additionally, we observed that the performance of the RFR-TEC map varies with the seasons, specifically showing higher errors in spring and autumn than in summer and winter.

Future research will focus on developing a comprehensive evaluation framework aimed at assessing the performance of our system across different latitudes and under varying levels of solar activity. This will further refine our understanding of the model's robustness and versatility in diverse geophysical contexts.

Conflict of Interest

The authors declare no conflicts of interest relevant to this study.

Data Availability Statement

The post-processed CODE GIM files can be downloaded from The Crustal Dynamics Data Information System (CDDIS) website (https://cddis.nasa.gov/archive/gnss/products/ionex/). The real-time UPC files with GIM ID "USRG" are publicly available for download at: https://chapman.upc.es/tomion/real-time/quick/archive.usrg/. The GNSS TEC products are provided by MIT Madrigal Database (http://millstonehill.haystack.mit.edu/). The GNSS RINEX observations are available at CDDIS website (https://cddis.nasa.gov/archive/gnss/data/daily/) and The Hong Kong Satellite Positioning Reference Station Network (https://www.geodetic.gov.hk/en/satref/satref. htm). The NASA JPL GIM TEC is available at https://sideshow.jpl.nasa.gov/pub/iono_daily/. The IRI-plas 2020 software is available at https://www.izmiran.ru/ionosphere/weather/grif/SPIM/. The source codes for this article are freely available on GitHub at: https://github.com/MengfeiSun95/RFR-TEC-Model (Sun, 2025).

References

Aa, E., Huang, W., Yu, S., Liu, S., Shi, L., Gong, J., et al. (2015). A regional ionospheric TEC mapping technique over China and adjacent areas on the basis of data assimilation. *Journal of Geophysical Research: Space Physics*, 120(6), 5049–5061. https://doi.org/10.1002/2015JA021140 Banville, S., Collins, P., Zhang, W., & Langley, R. B. (2014). Global and regional ionospheric corrections for faster PPP convergence. *Navigation*, 61(2), 115–124. https://doi.org/10.1002/navi.57

Banville, S., & Langley, R. B. (2013). Mitigating the impact of ionospheric cycle slips in GNSS observations. *Journal of Geodesy*, 87(2), 179–193. https://doi.org/10.1007/s00190-012-0604-1

Bilitza, D., Altadill, D., Truhlik, V., Shubin, V., Galkin, I., Reinisch, B., & Huang, X. (2017). International Reference Ionosphere 2016: From ionospheric climate to realtime weather predictions. *Space Weather*, 15(2), 418–429. https://doi.org/10.1002/2016sw001593

Bilitza, D., Altadill, D., Zhang, Y., Mertens, C., Truhlik, V., Richards, P., et al. (2014). The international reference ionosphere 2012–A model of international collaboration. *Journal of Space Weather and Space Climate*, 4, A07. https://doi.org/10.1051/swsc/2014004

Bilitza, D., Pezzopane, M., Truhlik, V., Altadill, D., Reinisch, B. W., & Pignalberi, A. (2022). The international reference ionosphere model: A review and description of an ionospheric benchmark. *Reviews of Geophysics*, 60(4), e2022RG000792. https://doi.org/10.1029/2022RG000792

Acknowledgments

This work was funded by the National Key Research and Development Program of China, Grant Number 2022YFD2401202; the National Key Research and Development Program of China, Grant Number 2022YFF0503904; the Guangdong Basic and Applied Basic Research Foundation, Grant Number 2022A1515010113; the Shenzhen Higher **Education Institutions Stabilization** Support Program Project, Grant Number GXWD20220811163556003; the National Key Laboratory of Electromagnetic Environment, Grant Number 202001004 and the Shenzhen Key Laboratory Launching Project Number ZDSYS20210702140800001

SUN ET AL. 14 of 16

1029/2024SW004237 by HONG KONG POLYTECHNIC UNIVERSITY HU NG HOM,

- Chen, J., Ren, X., Zhang, X., Zhang, J., & Huang, L. (2020). Assessment and validation of three ionospheric models (IRI-2016, NeQuick2, and IGS-GIM) from 2002 to 2018. Space Weather, 18(6), e2019SW002422. https://doi.org/10.1029/2019SW002422
- Chen, Z., Liao, W., Li, H., Wang, J., Deng, X., & Hong, S. (2022). Prediction of global ionospheric tec based on deep learning. *Space Weather*, 20(4), e2021SW002854. https://doi.org/10.1029/2021SW002854
- Chen, Fang, H., & Liu, Z. (2021). The application of a deep convolutional generative adversarial network on completing global TEC maps. Journal of Geophysical Research: Space Physics, 126(3), e2020JA028418. https://doi.org/10.1029/2020JA028418
- Chen, Jin, M., Deng, Y., Wang, J., Huang, H., Deng, X., & Huang, C. (2019). Improvement of a deep learning algorithm for total electron content maps: Image completion. *Journal of Geophysical Research: Space Physics*, 124(1), 790–800. https://doi.org/10.1029/2018JA026167
- Chen, Yi, W., Song, W., Shi, C., Lou, Y., & Cao, C. (2018). Evaluation of three ionospheric delay computation methods for ground-based GNSS receivers. GPS Solutions, 22(4), 125. https://doi.org/10.1007/s10291-018-0788-9
- Development of a regional GPS-based ionospheric TEC model for South Africa. (2007). Development of a regional GPS-based ionospheric TEC model for South Africa. Advances in Space Research, 39(5), 808–815. https://doi.org/10.1016/j.asr.2007.02.026
- Durazo, J., Kostelich, E. J., & Mahalov, A. (2021). Data assimilation for ionospheric space-weather forecasting in the presence of model Bias. Frontiers in Applied Mathematics and Statistics, 7, 679477. https://doi.org/10.3389/fams.2021.679477
- Eshkuvatov, H. E., Ahmedov, B. J., Tillayev, Y. A., Tariq, M. A., Shah, M. A., & Liu, L. (2023). Ionospheric precursors of strong earthquakes observed using six GNSS stations data during continuous five years (2011–2015). *Geodesy and Geodynamics*, 14(1), 65–79. https://doi.org/10.1016/j.geog.2022.04.002
- Forbes, J. M., Palo, S. E., & Zhang, X. (2000). Variability of the ionosphere. *Journal of Atmospheric and Solar-Terrestrial Physics*, 62(8), 685–693. https://doi.org/10.1016/S1364-6826(00)00029-8
- Gulyaeva, T., & Bilitza, D. (2012). New developments in the standard model (Vol. 1-39).
- Hernández-Pajares, M., Juan, J. M., & Sanz, J. (1999). New approaches in global ionospheric determination using ground GPS data. *Journal of Atmospheric and Solar-Terrestrial Physics*, 61(16), 1237–1247. https://doi.org/10.1016/S1364-6826(99)00054-1
- Hernández-Pajares, M., Juan, J. M., Sanz, J., Aragón-Àngel, À., García-Rigo, A., Salazar, D., & Escudero, M. (2011). The ionosphere: Effects, GPS modeling and the benefits for space geodetic techniques. *Journal of Geodesy*, 85(12), 887–907. https://doi.org/10.1007/s00190-011-0508-5
- Hernández-Pajares, M., Roma-Dollase, D., Krankowski, A., García-Rigo, A., & Orús-Pérez, R. (2017). Methodology and consistency of slant and vertical assessments for ionospheric electron content models. *Journal of Geodesy*, 91(12), 1405–1414. https://doi.org/10.1007/s00190-017-1032-z
- Hu, C., Chen, W., Chen, Y., Ding, X., & Simon, C.-w. K. (2001). Hong Kong GPS active network. In *International symposium on kinematic systems in geodesy, geomatics and navigation [KIS]*.
- Jehle, M., Ruegg, M., Zuberbuhler, L., Small, D., & Meier, E. (2009). Measurement of ionospheric faraday rotation in simulated and real spaceborne SAR data. *IEEE Transactions on Geoscience and Remote Sensing*, 47(5), 1512–1523. https://doi.org/10.1109/TGRS.2008.
- Ji, E.-Y., Moon, Y.-J., & Park, E. (2020). Improvement of IRI global TEC maps by deep learning based on conditional generative adversarial networks. Space Weather, 18(5), e2019SW002411. https://doi.org/10.1029/2019SW002411
- Jin, R., Jin, S., & Feng, G. (2012). M_DCB: Matlab code for estimating GNSS satellite and receiver differential code biases. GPS Solutions, 16(4), 541–548. https://doi.org/10.1007/s10291-012-0279-3
- Kong, Q., Qu, X., Zhang, S., Yin, F., Lu, R., & Chen, B. (2023). A secure satellite-edge computing framework for collaborative line outage identification in smart grid. IEEE Transactions on Services Computing, 17(3), 761–775. https://doi.org/10.1109/TSC.2023.3322432
- Kong, Q., Wang, Y., Zhang, S., Chen, B., Xiao, S., Bao, H., & Shao, J. (2024). Achieving secure on-orbit comparison in leo satellite-enabled offshore wind farm surveillance. *IEEE Internet of Things Journal*, 11(23), 38790–38802. https://doi.org/10.1109/JIOT.2024.3454765
- Kouba, J. (2009). A guide to using international GNSS service (IGS) products. Retrieved from http://igscb.jpl.nasa.gov/igscb/resource/pubs/UsingIGSProductsVer21.pdf
- Li, J., Wang, N., Zhang, L., Du, B., & Tao, D. (2020). Recurrent feature reasoning for image inpainting. In 2020 IEEE/CVF Conference on Computer Vision and Pattern Recognition (CVPR) (pp. 7757–7765). https://doi.org/10.1109/CVPR42600.2020.00778
- Li, Z., Wang, N., Hernández-Pajares, M., Yuan, Y., Krankowski, A., Liu, A., et al. (2020). IGS real-time service for global ionospheric total electron content modeling. *Journal of Geodesy*, 94(3), 32. https://doi.org/10.1007/s00190-020-01360-0
- Li, Huang, J., Li, X., Shen, Z., Han, J., Li, L., & Wang, B. (2022). Review of PPP–RTK: Achievements, challenges, and opportunities. *Satellite Navigation*, 3(1), 28. https://doi.org/10.1186/s43020-022-00089-9
- Lim, B. J. M., & Leong, E. C. (2019). Challenges in the detection of ionospheric Pre-earthquake total electron content anomalies (PETA) for earthquake forewarning. *Pure and Applied Geophysics*, 176(6), 2425–2449. https://doi.org/10.1007/s00024-018-2083-7
- Liu, G., Reda, F. A., Shih, K. J., Wang, T.-C., Tao, A., & Catanzaro, B. (2018). Image inpainting for irregular holes using partial convolutions. In *Proceedings of the european conference on computer vision (eccv)* (pp. 85–100).
- Liu, Z., & Gao, Y. (2004). Ionospheric tec predictions over a local area gps reference network. GPS Solutions, 8(1), 23–29. https://doi.org/10.1007/s10291-004-0082-x
- Liu, Chen, R., Wang, Z., & Zhang, H. (2011). Spherical cap harmonic model for mapping and predicting regional TEC. GPS Solutions, 15(2), 109–119. https://doi.org/10.1007/s10291-010-0174-8
- Liu, Zhang, B., Yuan, Y., & Li, M. (2018a). Real-time precise point positioning (rtppp) with raw observations and its application in real-time regional ionospheric vtec modeling. *Journal of Geodesy*, 92(11), 1267–1283. https://doi.org/10.1007/s00190-018-1118-2
- Li, Wang, N., Wang, L., Liu, A., Yuan, H., & Zhang, K. (2019). Regional ionospheric TEC modeling based on a two-layer spherical harmonic approximation for real-time single-frequency PPP. *Journal of Geodesy*, 93(9), 1659–1671. https://doi.org/10.1007/s00190-019-01275-5
- Ma, G., & Maruyama, T. (2003). Derivation of TEC and estimation of instrumental biases from GEONET in Japan. *Annales Geophysicae*, 21(10), 2083–2093. https://doi.org/10.5194/angeo-21-2083-2003
- Mannucci, A. J., Iijima, B., Sparks, L., Pi, X., Wilson, B., & Lindqwister, U. (1999). Assessment of global TEC mapping using a three-dimensional electron density model. *Journal of Atmospheric and Solar-Terrestrial Physics*, 61(16), 1227–1236. https://doi.org/10.1016/S1364-6826(99)00053-X
- Mannucci, A. J., Iijima, B. A., Lindqwister, U. J., Pi, X., Sparks, L., & Wilson, B. D. (1999). GPS and ionosphere.
- Mannucci, A. J., Wilson, B. D., Yuan, D. N., Ho, C. H., Lindqwister, U. J., & Runge, T. F. (1998). A global mapping technique for GPS-derived ionospheric total electron content measurements. *Radio Science*, 33(3), 565–582. https://doi.org/10.1029/97RS02707
- Mendoza, L. P. O., Meza, A. M., & Aragón Paz, J. M. (2019). A multi-GNSS, multifrequency, and near-real-time ionospheric TEC monitoring system for South America. Space Weather, 17(5), 654–661. https://doi.org/10.1029/2019SW002187

SUN ET AL. 15 of 16

Pan, Jin, M., Zhang, S., & Deng, Y. (2020). Tec map completion using DCGAN and Poisson blending. Space Weather, 18(5), e2019SW002390. https://doi.org/10.1029/2019SW002390

Pan, Jin, M., Zhang, S., & Deng, Y. (2021). Tec map completion through a deep learning model: Snpgan. Space Weather, 19(11), e2021SW002810. https://doi.org/10.1029/2021SW002810

Paszke, A., Gross, S., Massa, F., Lerer, A., Bradbury, J., Chanan, G., et al. (2019). Pytorch: An imperative style, high-performance deep learning library. Advances in Neural Information Processing Systems, 32.

Rideout, W., & Coster, A. (2006). Automated GPS processing for global total electron content data. GPS Solutions, 10(3), 219–228. https://doi.org/10.1007/s10291-006-0029-5

Roma-Dollase, D., Hernández-Pajares, M., Krankowski, A., Kotulak, K., Ghoddousi-Fard, R., Yuan, Y., et al. (2018). Consistency of seven different GNSS global ionospheric mapping techniques during one solar cycle. *Journal of Geodesy*, 92(6), 691–706. https://doi.org/10.1007/s00190-017-1088-9

Schaer, S. (1999). Mapping and predicting the Earth's ionosphere using the global positioning system. Retrieved from https://api.semanticscholar.org/CorpusID:128725332

Silva, A., Moraes, A., Sousasantos, J., Maximo, M., Vani, B., & Faria, C. (2023). Using deep learning to map ionospheric total electron content over Brazil. *Remote Sensing*, 15(2), 412. https://doi.org/10.3390/rs15020412

Song, F., & Shi, S. (2024). Improved ionospheric total electron content maps over China using spatial gridding approach. *Atmosphere*, 15(3), 351. https://doi.org/10.3390/atmos15030351

Sun, M. (2025). RFR-TEC-Model: RFR-TEC-model. Zenodo. https://doi.org/10.5281/zenodo.15834317

Takahashi, H., Wrasse, C. M., Denardini, C. M., Pádua, M. B., de Paula, E. R., Costa, S. M. A., et al. (2016). Ionospheric TEC weather map over South America. Space Weather. 14(11), 937–949. https://doi.org/10.1002/2016SW001474

Tariq, M. A., Shah, M., Hernández-Pajares, M., & Iqbal, T. (2019). Pre-earthquake ionospheric anomalies before three major earthquakes by GPS-TEC and GIM-TEC data during 2015–2017. Advances in Space Research, 63(7), 2088–2099. https://doi.org/10.1016/j.asr.2018.12.028

Tulasi Ram, S., Su, S.-Y., & Liu, C. (2009). Formosat-3/cosmic observations of seasonal and longitudinal variations of equatorial ionization anomaly and its interhemispheric asymmetry during the solar minimum period. *Journal of Geophysical Research*, 114(A6). https://doi.org/10.1007/s10291-004-0082-x

Vadakke Veettil, S., Aquino, M., Marques, H. A., & Moraes, A. (2020). Mitigation of ionospheric scintillation effects on GNSS precise point positioning (PPP) at low latitudes. *Journal of Geodesy*, 94(2), 15. https://doi.org/10.1007/s00190-020-01345-z

Yang, D., Fang, H., & Liu, Z. (2022). Completion of global ionospheric TEC maps using a deep learning approach. *Journal of Geophysical Research: Space Physics*, 127(5), e2022JA030326. https://doi.org/10.1029/2022JA030326

Yu, J., Lin, Z., Yang, J., Shen, X., Lu, X., & Huang, T. S. (2018). Generative Image Inpainting With Contextual Attention. In (pp. 5505–5514).
Zhang, B. (2016). Three methods to retrieve slant total electron content measurements from ground-based GPS receivers and performance assessment. *Radio Science*, 51(7), 972–988. https://doi.org/10.1002/2015RS005916

Zhang, R., Li, H., Shen, Y., Yang, J., Li, W., Zhao, D., & Hu, A. (2025). Deep learning applications in ionospheric modeling: Progress, challenges, and opportunities. *Remote Sensing*, 17(1), 124. https://doi.org/10.3390/rs17010124

Zhou, C., Yang, L., Li, B., & Balz, T. (2022). M_GIM: A MATLAB-based software for multi-system global and regional ionospheric modeling. GPS Solutions, 27(1), 42. https://doi.org/10.1007/s10291-022-01370-9

SUN ET AL. 16 of 16